Journal of Hydrology 664 (2026) 134390

Contents lists available at ScienceDirect

Journal of Hydrology

journal homepage: www.elsevier.com/locate/jhydrol

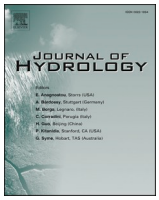

Research papers

Loss and recovery of terrestrial carbon sinks induced by 2020 extreme precipitation in the Yangtze River Valley

Zishan Wang [a,b], Jun Wang [a,b,*], Hao Zhou [c], Qixiang Cai [d], Ran Yan [a,b], Hongzhao Wang [a,b], Zhi Huang [a,b], Meirong Wang [e,f], Weimin Ju [a,b]

[a] International Institute for Earth System Science, Nanjing University, Nanjing, Jiangsu 210023, China
[b] Jiangsu Provincial Key Laboratory of Geographic Information Science and Technology, Key Laboratory for Land Satellite Remote Sensing Applications of Ministry of Natural Resources, School of Geography and Ocean Science, Nanjing University, Nanjing, Jiangsu 210023, China
[c] College of Meteorology and Oceanography, National University of Defense Technology, Changsha 410003, China
[d] Aerospace Information Research Institute, Chinese Academy of Sciences, Beijing 100094, China
[e] Joint Center for Data Assimilation Research and Applications/Key Laboratory of Meteorological Disaster, Ministry of Education/Joint International Research Laboratory of Climate and Environment Change (ILCEC)/Collaborative Innovation Center ON Forecast and Evaluation of Meteorological Disasters, Nanjing University of Information Science and Technology, Nanjing 210044, China
[f] Tibet Field Station for Scientific Observation and Research on Atmospheric Water Cycle in Mêdog/Xigazê and Mêdog National Climate Observatory, Tibet Meteorological Service, Lhasa 850000, China

ARTICLE INFO

This manuscript was handled by Dr Emmanouil Anagnostou, Editor-in-Chief, with the assistance of Xiaodong Zhang, Associate Editor

Keywords:
Terrestrial carbon sinks
Carbon loss and recovery
2020 extreme precipitation
Yangtze River Valley
Downward solar radiation

ABSTRACT

Extreme precipitation within the context of global climate change has dramatic impacts on terrestrial carbon sequestration. While extensive research has focused on the adverse impacts of droughts on terrestrial carbon sinks, the effects of extreme precipitation events remain underexplored. Here we investigated the carbon sink dynamics induced by a record-breaking heavy precipitation event over the Yangtze River Valley (YRV) in June-July (JJ) 2020, using OCO-2 v10 MIP posterior data and simulations from two terrestrial biosphere models (VEGAS and LPJwsl). Our results show that extreme precipitation in JJ caused a significant decline in net biome productivity (NBP), with reductions of approximately − 16.75 Tg C by OCO-2 v10 MIP, −23.50 Tg C by VEGAS, and − 16.88 Tg C by LPJwsl, predominantly driven by substantial decreases in gross primary production (GPP). Following the cessation of precipitation in August, negative NBP anomalies persisted due to stronger total ecosystem respiration (TER*), but rapid recovery was observed, with recovery rates of 55.40 %, 83.58 %, and 86.85 %, respectively, driven by a resurgence in GPP. Extreme precipitation also triggered significant variations in temperature, soil moisture, surface downward solar radiation (RAD), and vapor pressure deficit (VPD), all of which influenced NBP. Attribution analysis revealed reduced RAD as the primary factor behind negative NBP anomalies during JJ, with contributions of approximately − 19.36 Tg C in VEGAS and − 8.54 Tg C in LPJwsl. In August, VEGAS emphasized negative legacy effects from JJ, while LPJwsl pointed to the suppressive role of high temperatures. Furthermore, both models consistently underscored the pivotal role of RAD in carbon sink recovery. Considering the increasing frequency and intensity of heavy precipitation under global warming, our study emphasized the negative effects of extreme precipitation on the terrestrial carbon sequestration, providing the further understanding on interactions of extreme climatic events and terrestrial ecosystems.

1. Introduction

The intensification of global water cycle has led to increased average precipitation and greater variability in precipitation patterns (Allen and Ingram, 2002; Zhang et al., 2021). Furthermore, extreme precipitation events, characterized by intense rainfall delivered in a single event, are projected to become more frequent and intense throughout the 21st century (Pendergrass and Hartmann, 2014; Donat et al., 2016; Giorgi et al., 2019; Intergovernmental Panel on Climate, 2023). Recent notable heavy rainfall events include the Midwest US in 2019 (Ford et al., 2021), western Europe in July 2019 (Cornwall, 2021), and southeastern Brazil in 2020 (Dalagnol et al., 2022), all of which resulted in devastating

* Corresponding author at: International Institute for Earth System Science, Nanjing University, Nanjing, Jiangsu 210023, China.
E-mail address: wangjun@nju.edu.cn (J. Wang).

https://doi.org/10.1016/j.jhydrol.2025.134390
Received 15 January 2025; Received in revised form 16 September 2025; Accepted 5 October 2025
Available online 12 October 2025

environmental consequences. Ecosystem productivity and carbon sequestration are increasingly threatened by the rising frequency of extreme hydroclimatic events in a warming climate (Chen et al., 2019a; Yin et al., 2020). Thus, understanding the response of terrestrial carbon sequestration to extreme precipitation is critical for predicting the impacts of climate change on global terrestrial ecosystems.

Precipitation regulates soil water availability, reduces surface temperature (TAS) and vapor pressure deficit (VPD), and decreases downward solar radiation (RAD) due to high cloud coverage during events, thereby influencing terrestrial vegetation growth and carbon cycle (Knapp et al., 2002; Zeppel et al., 2014). The impacts of extreme precipitation on terrestrial ecosystem carbon sequestration depend on vegetation type as well as event timing (Balashov et al., 2023). Ma et al. (2016) observed that Australian grasslands can thrive under anomalously wet conditions, assimilating more carbon than under normal soil moisture levels. In contrast, croplands are highly susceptible to waterlogging and have a tendency to be net sources of atmospheric CO_2 during flooding (Ahmed et al., 2013; Yildirim and Demir, 2022). The widespread flooding in the US Midwest during spring and early summer 2019 caused a notable reduction of approximately 0.1 Pg C in cropland net ecosystem exchange (NEE) during June and July. Compared to 2017 and 2018, these anomalously wet conditions resulted in a 15 %–25 % decrease in annual net carbon uptake. Although rainstorms often lead to crop failures, they may also alleviate water shortages, enhancing crop production under specific conditions (Chen et al., 2019a). Intense precipitation events, however, can erode topsoil, transferring particulate and dissolved organic carbon (DOC) from terrestrial to riverine ecosystems (Dinsmore et al., 2013; Hilton et al., 2008). However, such impacts of extreme precipitation on the terrestrial ecosystem carbon cycle remains unquantified (Piao et al., 2019).

The middle and lower reaches of Yangtze River Valley (YRV) are the vital industrial and agricultural zones, as well as densely populated areas in China. Accumulated Meiyu rainfall accounts for 45 % of summer precipitation in this area (Ding, 2004; Zhang, 2015; Zhang et al., 2023; Zhang et al., 2017; Chen et al., 2019b). Over the past four decades, the region has experienced several record-breaking Meiyu rainfall events with considerable ecological damage. In the summer of 1998, rainfall levels nearly matched the record set in 1954. In early summer 2020, an extreme Meiyu event produced the highest precipitation levels since 1961, surpassing those of 1998 (Wang et al., 2022). This event featured unprecedented precipitation accumulation, the longest duration, the earliest onset, and the highest intensity, causing human loss, vegetation mortality, and property damage (Liu et al., 2023). Although the atmospheric circulation and moisture dynamics of the 2020 event have been analyzed by extensive studies (Pan et al., 2021; Chen et al., 2022; Qi et al., 2023), its effects on terrestrial carbon sinks and the driving factors remain unclear.

In order to better understand the effects of climate extremes on carbon exchange between terrestrial ecosystems and the atmosphere, we here analyzed carbon sink dynamics and underlying driving mechanisms following the record-breaking precipitation event of 2020. Using net biome productivity (NBP) data simulated by the VEGAS and LPJwsl models, optimized through atmospheric inversions from the OCO-2 v10 MIP, and supplemented with simulated and satellite-derived GPP products, we examined NBP anomalies, the contributions of different biological processes (photosynthesis and respiration), and the key climatic factors driving NBP variations.

2. Materials and methods

2.1. Climate datasets

In this study, we used Integrated Multi-satellite Retrievals for GPM (IMERG) precipitation data from 2001 to 2023, with a temporal resolution of one month and a spatial resolution of 0.1°× 0.1°. Designed to deliver accurate and reliable global precipitation estimates by integrating all available sensors from TRMM and GPM eras, IMERG combines the strengths of CMORPH, PERSAINN and TMPA products (Anjum et al., 2018; Prakash, 2019). Previous studies have demonstrated that IMERG products outperforms other satellite precipitation datasets, such as TRMM 3B42, 3B42RT and PERSIANN-CDR, in terms of accuracy and precipitation detection across diverse regions (Yu et al., 2021).

Meteorological variables, including 2 m dewpoint temperature (TD), TAS, RAD, and soil moisture (SM), were sourced from the fifth-generation European Centre for Medium-Range Weather Forecasts (ECMWF) atmospheric reanalysis of global climate (ERA5-Land) for the period 2001–2020 (Muñoz-Sabater et al., 2021). ERA5-Land is a high-resolution dataset created by replaying the land component of the ECMWF ERA5 climate reanalysis. It merges observational data and physical models to produce a globally complete and consistent dataset with a spatial resolution of 0.1°× 0.1°.

VPD was calculated according to the following formula, as described by Wang et al. (2023):

$$VPD = 0.61078 \times \left(e^{\frac{17.27 \times TAS}{TAS+237.29}} - e^{\frac{17.27 \times TD}{TD+237.29}} \right) \quad (1)$$

where TAS and TD are measured in degrees Celsius, and the derived VPD is expressed in kilopascals (kPa). Based on the recommendation of He et al. (2022), we used monthly TAS and TD data to compute VPD, as monthly and daily ERA5-derived VPD anomalies were found to be nearly identical.

SM data offer detailed soil moisture information across three depth layers: 0–7 cm, 7–28 cm, and 28–100 cm. A weighted average was employed to calculate SM for the 0–100 cm layer (Muñoz-Sabater et al., 2021). The ERA5-Land soil moisture dataset has undergone rigorous validation using in situ observations from the Global Hydrological Network, demonstrating high accuracy for both surface and root-zone soil moisture (Li et al., 2020; Li and Xiao, 2020; Walther et al., 2019). It has been widely used in studies analyzing vegetation water availability (Fan et al., 2022; Jiao et al., 2021; Li et al., 2022).

To ensure compatibility with the following carbon cycle-related variables, all climate datasets were interpolated into a spatial resolution of 0.5° × 0.5° for subsequent analyses.

2.2. Terrestrial biosphere model simulations

In this study, we utilized simulations from two widely used Terrestrial Biosphere Models (TBMs), namely Vegetation-Global Atmosphere-Soil (VEGAS) version 2.6 (Zeng et al., 2005) and Lund-Potsdam-Jena-Wald, Schnee, Landschaft (LPJwsl) (Sitch et al., 2003), to explore the NBP changes under extreme precipitation event in 2020. Both VEGAS and LPJwsl have been extensively applied to investigate global and regional terrestrial carbon cycles, focusing on seasonal cycle, interannual variability, and long-term changes (Qian et al., 2008; Sitch et al., 2015; Wang et al., 2016; Wang et al., 2018b). The latest version of VEGAS includes an improved parametrization of crop modeling, incorporating the intensification of agriculture due to the Green Revolution. This new crop module simulates the behavior of three dominant crops (maize, wheat, and rice) with a generic crop function type (Zeng et al., 2014). LPJwsl simulates ecosystem carbon, water, and energy fluxes by linking multiple mechanistic and partially empirical submodels (Wang et al., 2018a). Additionally, LPJwsl provides estimates of GPP that align closely with the average GPP values from a critical assessment of 45 global GPP products (Zhang and Ye, 2021).

We ran these two TBMs with time-variant datasets for CO_2, climate, and land-use changes at a spatial resolution of 0.5°×0.5° from 1901 to the present. Climate data were generated by combining the Climatic Research Unit (CRU) Time-series (TS) monthly product (Harris et al., 2020) with the fifth generation ECMWF atmospheric reanalysis (ERA5) hourly datasets (Hersbach et al., 2020). The gridded cropland and

pasture land-use datasets were derived from the History Database of the Global Environment (HYDE) (Goldewijk, 2017). To ensure equilibrium in the carbon pools, the models were spun up using the forcing data from 1901 to 1910 over a 500-year period.

In this study, we used NBP to represent the carbon sources and sinks over the YRV, defined as:

$$NBP = GPP - TER - D \quad (2)$$

where GPP is the gross primary production, TER is the total ecosystem respiration, and D denotes disturbance-induced carbon fluxes, encompassing grazing, harvest, land-use change, and wildfires here (Poulter et al., 2011; Sitch et al., 2003; Zeng et al., 2005; Zhang et al., 2018). Since the processes considered by the two models differ, for simplicity, we combine the terms TER and D into a single term, TER*, for the following analyses:

$$NBP = GPP - TER^{*} \quad (3)$$

2.3. OCO-2 v10 MIP products

The OCO-2 Model Intercomparison Project (OCO-2 MIP) is a collaborative effort among atmospheric CO_2 modelers to study the impact of assimilating OCO-2 retrievals into atmospheric inversion models (Byrne et al., 2022). This study utilized NBP products derived from 13 atmospheric inversion models (as detailed in Table S1) within the OCO-2 v10 MIP. Modelers performed a standard suite of inversion experiments, using a prescribed common fossil fuel emission dataset but independent prior surface carbon fluxes, which were constrained by CO_2 observations from OCO-2 and in situ measurements. The commonly used fossil fuel emission adopted the Open-source Data Inventory for Anthropogenic CO_2 (ODIAC) emission data product (Oda et al., 2018), which provides monthly gridded emissions at a $1^{\circ} \times 1^{\circ}$ resolution up to 2019, and extrapolated emissions in 2020 with additional information from the Carbon Monitor emission product. In addition, ODIAC 2020 is employed in the OCO-2 MIP for atmospheric CO_2 modeling (Basu and Nassar, 2021). For fire emissions, most models used the Global Fire Emission Database, either version 3 (GFED3) or version 4 (GFED4) (Peiro et al., 2022). The project consists of four experiments: (a) IS: Assimilation of in situ CO_2 measurements from an international observational network; (b) LNLG: Assimilation of OCO-2 ACOS v10 land nadir and land glint XCO_2 retrievals; (c) LNLGIS: Assimilation of in situ CO_2 measurements and OCO-2 ACOS v10 land nadir and land glint XCO_2 retrievals; (d) LNLGOGIS: Assimilation of in situ CO_2, measurements and all OCO-2 retrievals. In this study, we adopted the ensemble mean of results from the LNLGOGIS experiment.

2.4. Satellite-based GPP product

In the main text, we utilized the Moderate Resolution Imaging Spectroradiometer (MODIS) Terra GPP data, an 8-day cumulative composite with a spatial resolution of 500 m, covering the period from 2001 to 2020. The GPP estimation in this dataset is based on the MOD17 algorithm, which employs a simple light use efficiency (LUE) model. This algorithm calculates GPP using biome-specific parameters and daily environmental inputs, including incoming photosynthetically active radiation (PAR), minimum temperature over a 24-hour period, and average daytime VPD (Turner et al., 2006). This dataset provides a widely used, high-resolution measure of vegetation productivity, enabling a detailed analysis of terrestrial carbon dynamics and their response to climatic and environmental changes.

Additionally, we also utilized the solar-induced fluorescence (SIF) from TROPOSIF dataset to examine vegetation changes from JJ to August. SIF is the near-infrared light re-emitted from illuminated plants and it has been found to strongly correlate with GPP (Guanter et al., 2014; Köhler et al., 2018; Wang et al., 2021). We used the daily ungraded (L2B) TROPOSIF data derived from the 743–758 nm window, which provides unprecedented high spatial and near-daily global coverage (Köhler et al., 2020), to generate gridded monthly SIF and DCSIF with a spatial resolution of 0.5° from 2018 to 2020.

2.5. Observation site

In this study, we further used data on NEP, GPP and TER observed through eddy covariance at the Jinfo mountain site of the ChinaFLUX network to validate changes in carbon fluxes. The quality of the data was high, with the proportion of valid half-hourly CO_2 flux observations ranging from 80.93 % to 86.47 %. The flux observation tower, situated at the Lanbaqing natural secondary forest observation site within the Jinfo mountain National Station (107.1508°E, 29.0217°N), has been in operation since late 2019. It is equipped with a state-of-the-art CPEC310 closed-path eddy covariance system, which is specifically designed for accurate and long-term monitoring of CO_2, water, and energy fluxes within the atmospheric boundary layer.

2.6. Annual rice yield data

The provinces of YRV mainly practice double-cropping systems, including rice–wheat, rice-rapeseed, and rice-vegetables rotations. Typically, rice is sown in May, transplanted in June, and harvested in October, with other crops planted during the remainder of the year (Zhang et al., 2015). As such, the extreme precipitation in June and July (JJ) may influence rice growth, potentially affecting annual rice yields. In this study, we retrieved province-level statistics for the annual rice production for 2019 and 2020 to analyze the potential impacts of this extreme precipitation. Specifically, the year-on-year (YoY) percentage change in rice production was calculated using the following formula:

$$YoY = \frac{RiceYield_{2020} - RiceYield_{2019}}{RiceYield_{2019}} \times 100\% \quad (4)$$

where $RiceYield_{2019}$ and $RiceYield_{2020}$ denote the annual rice productions in 2019 and 2020, respectively. The YoY value is expressed as a percentage (%), with a positive value indicating an increase in rice production relative to 2019 and a negative value indicating a decrease.

2.7. Calculations of detrended anomalies of climate variables and carbon fluxes

The analyses in this study were based on the detrended anomalies of monthly climate and carbon fluxes. Specifically, for each grid cell, the following steps were applied: (1) The climatological monthly mean of the carbon fluxes (NBP, GPP, and TER*) and climate drivers (TAS, RAD, SM, and VPD) was subtracted to eliminate the effect of seasonal cycle. (2) To eliminate the effects of long-term changes such as those induced by climate warming, CO_2 fertilization, and other factors, the linear trends for each grid cell from 2001 to 2020 were subtracted. This step ensured that the analyses focused on short-term anomalies rather than long-term trends. This approach helped isolate the short-term variations in carbon fluxes and climate drivers, which were critical for understanding the immediate impacts of extreme precipitation events.

2.8. Degree of recovery

Considering that extreme precipitation in 2020 primarily occurred in June and July (JJ), which was predominantly concentrated in the YRV, we computed the average of JJ as a single month for all subsequent analyses. By comparing the anomalous NBP in August to the average anomalous NBP for JJ, we can quantify the percentage of NBP recovery across different data products. In detail, the degree of recovery (DoR) can be expressed by the formula:

$$DoR = \left(1 - \frac{\Delta NBP_{August}}{\Delta NBP_{AverageofJuneandJuly}}\right) \times 100\% \quad (5)$$

where ΔNBP_{August} and $\Delta NBP_{AverageofJuneandJuly}$ are the total amount of anomalous NBP in August and JJ within the study area (Tg C mo^{-1}). Since we have noticed that ecosystem carbon sequestration markedly declined during the extreme precipitation but subsequently recovered or even increased after the event subsided, a higher DoR in Equation (5) indicates a stronger recovery of ecosystem carbon sequestration. When DoR exceeds 1, it suggests not only complete offset of the negative impacts of extreme precipitation but also a net increase in sequestration.

2.9. Climate attribution of NBP anomalies

To assess the sensitivity of ecosystem carbon sinks to climate fluctuations (including TAS, RAD, SM, and VPD), we constructed a multiple linear regression (MLR) model at each pixel within the study area to isolate the individual contributions of climate drivers to NBP anomalies, while accounting for the legacy effect of NBP from the previous months. The model is expressed as follows:

$$NBP_c = \beta_1 NBP_p + \beta_2 TAS + \beta_3 RAD + \beta_4 SM + \beta_5 VPD + \epsilon \quad (6)$$

Where NBP_c and NBP_p are the detrended NBP anomalies in the current and previous months (gC m^{-2} mo^{-1}), respectively; *TAS*, *RAD*, *SM* and *VPD* represent detrended anomalies of the corresponding meteorological variables for the current month. The regression coefficients β_1, β_2, β_3, β_4, and β_5 represent the apparent sensitivities of NBP to the legacy effect of previous NBP, TAS, RAD, SM and VPD, respectively, and ϵ is the residual error term. These coefficients are estimated using Ordinary Least Squares (OLS). To quantify the contribution of each factor, we multiplied its regression coefficient by the corresponding climate anomalies for June–July (JJ) and August 2020, then summed the values of all pixels to obtain total predicted NBP anomalies. Model performance was assessed using R-squared (Multiple R^2). Additionally, we treated the entire region as a single entity to construct a MLR model, ensuring the

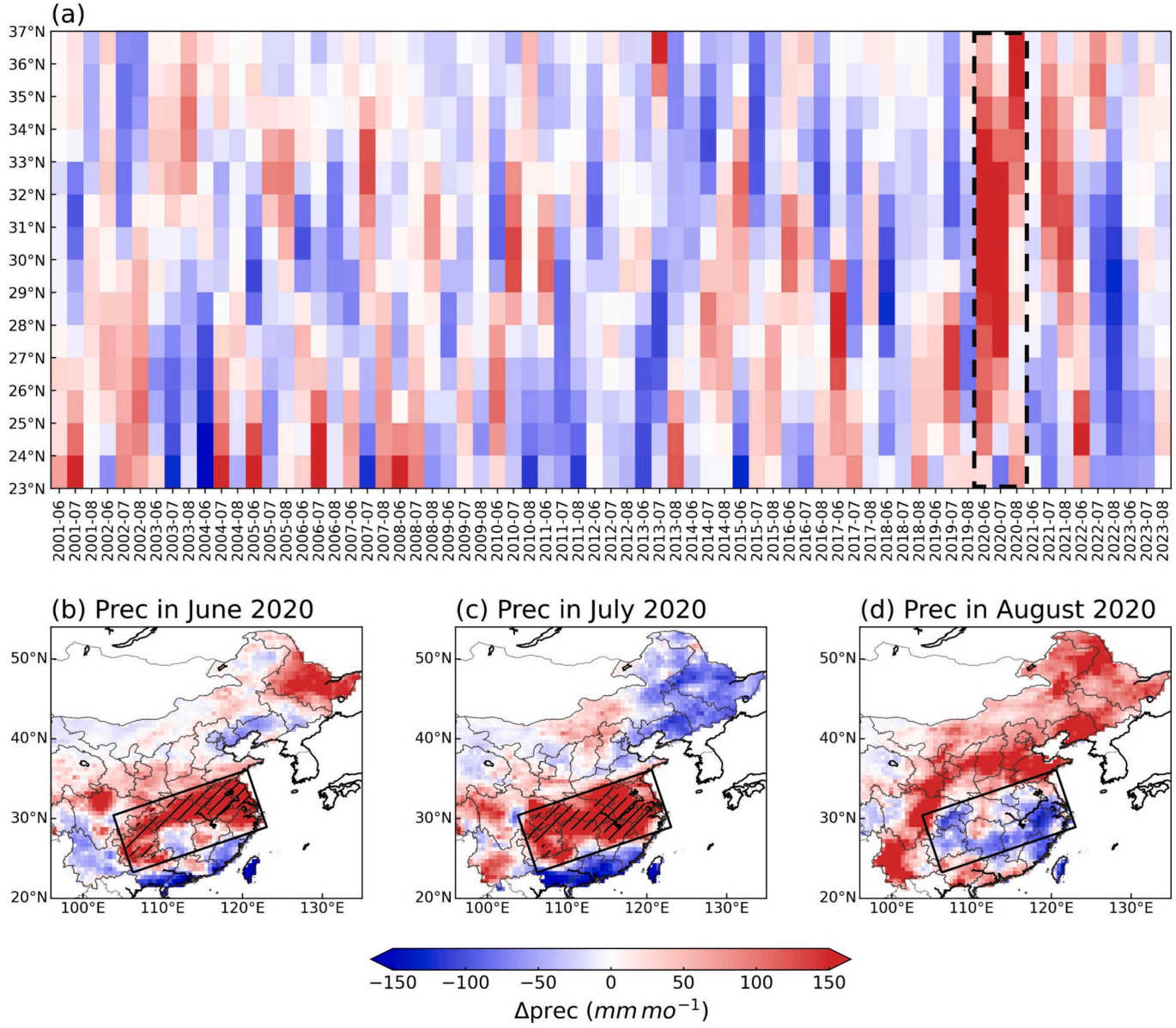

Fig. 1. Detrended precipitation anomalies. (a) Latitudinal mean of detrended land precipitation anomalies (104°E–124°E) for summer months (June–August) from 2001 to 2023. Panels (b), (c), and (d) display the spatial distributions of precipitation anomalies for June, July, and August, respectively. Precipitation is expressed in mm mo^{-1}. Hatched areas represent pixels where anomalies exceed twice the standard deviation over the past 19 years. The black box outlines the study region.

robustness and consistency of the results.

3. Results

3.1. NBP anomalies induced by extreme precipitation in summer 2020

In the summer of 2020, record-breaking heavy rainfall affected southern China, particularly the middle and lower reaches of the YRV (Fig. 1). The latitudinal mean of land precipitation anomalies within the range of 104°E to 124°E from 2001 to 2023 shows that heavy precipitation in the YRV during June and July of 2020 was the most severe in the past two decades (Fig. 1a). Spatially, most provinces within the YRV experienced prolonged rainfall, with 41.2 % of areas in June and 48.6 % in July in the study region exceeding twice the standard deviation of precipitation for the corresponding months over the past 19 years (Figs. 1b and c). Precipitation subsequently declined in August as the rain belt shifted northward into North China (Fig. 1d).

Fig. 2 shows the variations in NBP, based on multiple atmospheric inversions from the OCO-2 v10 MIP and two terrestrial biosphere model simulations. Clearly, during JJ, NBP exhibited widespread negative anomalies across the study region (Fig. 2a-c). Observations from the Jinfo mountain site are consistent with the findings, exhibiting significant negative anomalies with NBP at − 11.63 gC m^{-2} mo^{-1} (Fig. 2a). Extreme precipitation event weakened the terrestrial carbon sink, exhibiting consistency across regional and site scales. However, spatial patterns of strong negative anomalies vary to some extent, likely due to differences in underlying factors. For example, OCO-2 v10 MIP results are influenced by prior flux error settings, atmospheric transport models, meteorological inputs, optimization techniques, and observational data quality (Basu et al., 2018; Chevallier et al., 2010; Schuh et al., 2019). In contrast, TBM simulations are shaped by model structures, included processes, and parameterizations (Rogers et al., 2014; Rogers, 2014).

By August, as precipitation subsided, negative NBP anomalies weakened (Fig. 2d–f), and some regions even showed positive anomalies (Figs. 2e and f). At the Jinfo mountain site, observations reveal a recovery in carbon sink capacity, with NBP rebounding to 9.14 gC m^{-2} mo^{-1} (Fig. 2d).

3.2. Underlying biological processes

According to Equation (3), NBP anomalies are determined by GPP and TER*. To better understand these contributions, we analyzed their variations (Fig. 3). It is important to note that OCO-2 v10 MIP directly optimizes NBP without explicitly accounting for GPP and TER*. Thus, our analysis primarily focused on the results from the two TBM simulations. Obviously, both VEGAS and LPJwsl simulations showed a marked and widespread GPP decline during JJ (Figs. 3b and c), mirroring the patterns of NBP anomalies (Figs. 2b and c). This decline is further supported by MODIS GPP data (Fig. 3a). The spatial patterns of SIF and DCSIF also reveal significant negative anomalies in the Northeast and Southwest regions of the study area (Figs. S1a and b). At the Jinfo mountain site, the negative GPP anomalies are particularly pronounced, with a value of − 44.60 gC m^{-2} mo^{-1} (Fig. 3c). Meanwhile, TER* exhibited a slight increase, implying that GPP variations were the primary drivers of NBP changes (Figs. 2b and c). In contrast, TER* at the Jinfo mountain site exhibited negative anomalies, measured at − 32.97 gC m^{-2} mo^{-1} (Fig. 3e).

In August, GPP demonstrated a clear recovery, particularly in the VEGAS and MODIS data, which showed widespread increases (Fig. 3f-h). Compared to JJ, the negative anomalies in SIF and DCSIF have been alleviated, with positive anomalies being more prevalent (Figs. S1c and

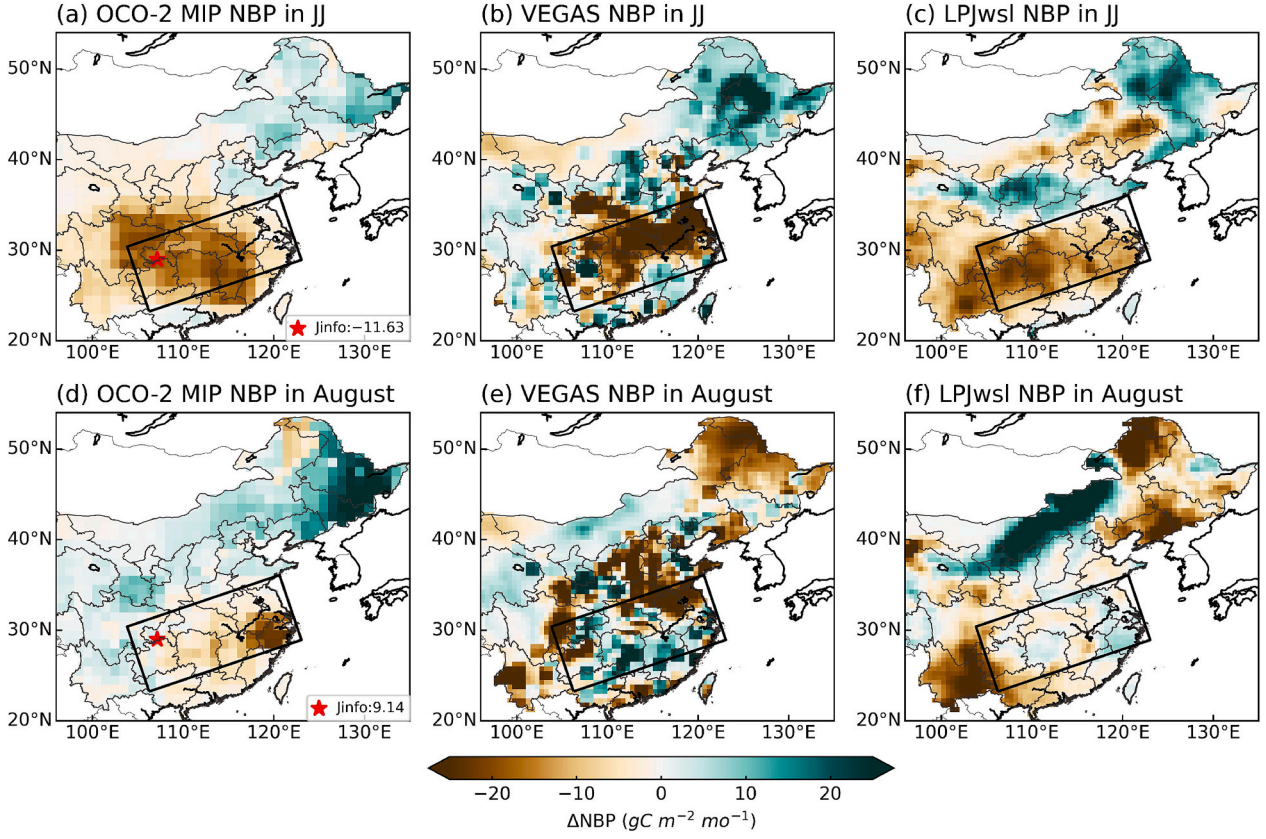

Fig. 2. Detrended NBP anomalies. (a–c) show mean June-July (JJ) NBP anomalies for OCO-2 v10 MIP, VEGAS and LPJwsl, respectively. (d–f) illustrate August NBP anomalies for OCO-2 v10 MIP, VEGAS, and LPJwsl, respectively. NBP is expressed in gC m^{-2} mo^{-1}. The red star represents the observed NBP anomalies at the Jinfo mountain site. (For interpretation of the references to colour in this figure legend, the reader is referred to the web version of this article.)

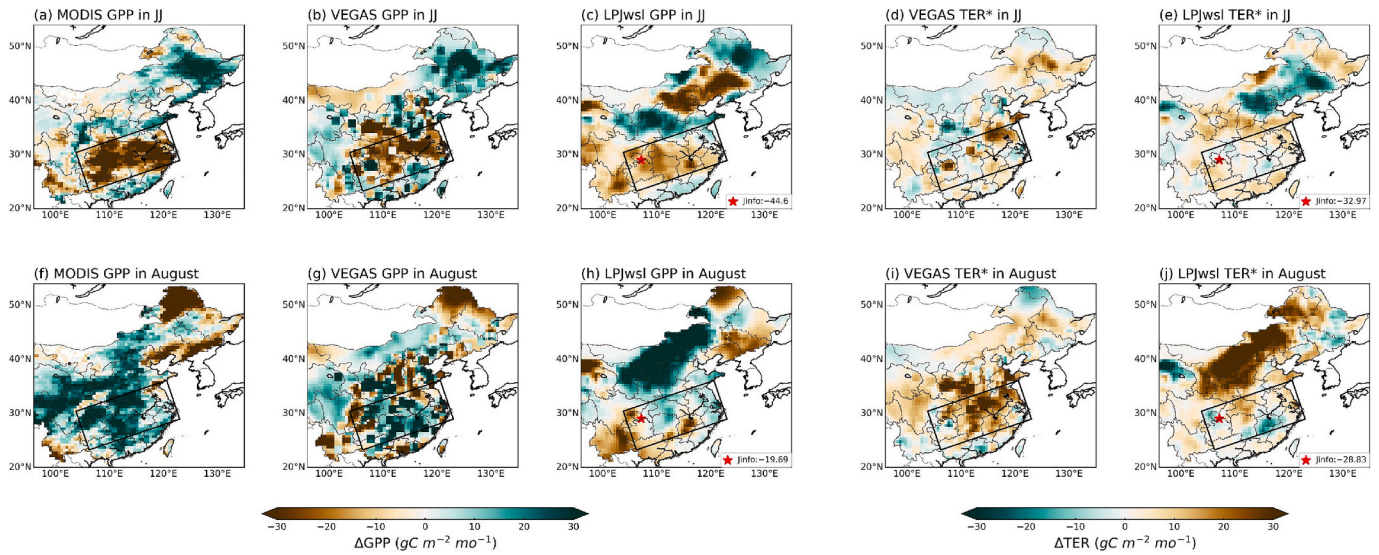

Fig. 3. Detrended GPP and TER* anomalies. (a-c) show mean GPP anomalies during JJ for MODIS, VEGAS and LPJwsl, respectively. (d-e) show mean TER* anomalies during JJ for VEGAS and LPJwsl, respectively. (f-h) represent GPP anomalies in August for MODIS, VEGAS, and LPJwsl, respectively. While (i-j) represent TER* anomalies in August for VEGAS, and LPJwsl, respectively. GPP and TER* are expressed in gC m^{-2} mo^{-1}. The red star indicates observed GPP and TER* anomalies at the Jinfo mountain site. (For interpretation of the references to colour in this figure legend, the reader is referred to the web version of this article.)

d). At the Jinfo mountain site, GPP remains negative at − 19.69 gC m^{-2} mo^{-1}, but this represents notable recovery compared to the stronger negative anomaly of − 44.60 gC m^{-2} mo^{-1} observed in JJ (Fig. 3h). Additionally, TER* increases in some regions relative to JJ, with a more pronounced enhancement observed in the VEGAS model (Figs. 3i and j).

In order to quantitatively analyze carbon sink dynamics, we computed the regional total anomalies of NBP, GPP, and TER* (Fig. 4). Significant negative NBP anomalies were observed in JJ, with values of approximately − 16.75 Tg C in OCO-2 v10 MIP, −23.50 Tg C in VEGAS, and − 16.88 Tg C in LPJwsl (Fig. 4a). Concurrently, GPP exhibited negative anomalies of − 17.50 Tg C in VEGAS and − 11.29 Tg C in LPJwsl, predominantly accounting for 74.47 % and 66.88 % of the NBP variations, respectively. The GPP reductions were confirmed but were less pronounced compared to MODIS GPP, which recorded a larger negative anomaly of − 32.47 Tg C. In contrast, TER* exhibited positive anomalies, with magnitudes of 6 Tg C in VEGAS and 5.59 Tg C in LPJwsl (Fig. 4a). Compared with NBP and GPP, the disturbance terms incorporated into TER* were negligible in magnitude, with values of − 0.52 Tg C in VEGAS and − 0.68 Tg C in LPJwsl.

In August, as precipitation subsided, spatial patterns revealed some positive anomalies, particularly in VEGAS (Fig. 2e). However, total NBP anomalies remained negative, with values of approximately − 7.47 Tg C in OCO-2 v10 MIP, −3.85 Tg C in VEGAS, and − 2.22 Tg C in LPJwsl (Fig. 4b). Compared to the apparent reduced GPP in JJ, GPP in August showed obvious increases of 12.59 Tg C in VEGAS and 23.52 Tg C in MODIS, while LPJwsl exhibited a near-neutral change (−0.06 Tg C). Meanwhile, TER* maintained positive anomalies in total, with magnitudes of 16.44 Tg C in VEGAS and 2.16 Tg C in LPJwsl (Fig. 4b). This suggests that positive TER* anomalies significantly contributed to sustaining the negative NBP anomalies observed in August.

Using Equation (5), we quantified the DoR for NBP in August compared to JJ, with values of approximately 55.40 % for OCO-2 MIP, 83.58 % for VEGAS, and 86.85 % for LPJwsl. The analysis highlights that NBP recovery was primarily driven by changes in GPP. Total GPP anomalies showed substantial increases compared to JJ, shifting from − 32.47 Tg C to 23.52 Tg C for MODIS, −17.50 Tg C to 12.59 Tg C for VEGAS, and − 11.29 Tg C to − 0.06 Tg C for LPJwsl. Although TER* also exhibited changes in both TBMs, the magnitudes of these changes were notably smaller compared to those of GPP. Meanwhile, the disturbance remained negative but exhibited a slight increase relative to JJ, as confirmed by − 0.17 Tg C for VEGAS and − 0.23 Tg C for LPJwsl. Besides, the mean anomalies of SIF and DCSIF confirmed a significant increase in GPP from JJ to August, with an increase of 18.01 mW m^{-2} μm^{-1} sr^{-1} for SIF and 4.76 mW m^{-2} μm^{-1} sr^{-1} for DCSIF (Fig. S1).

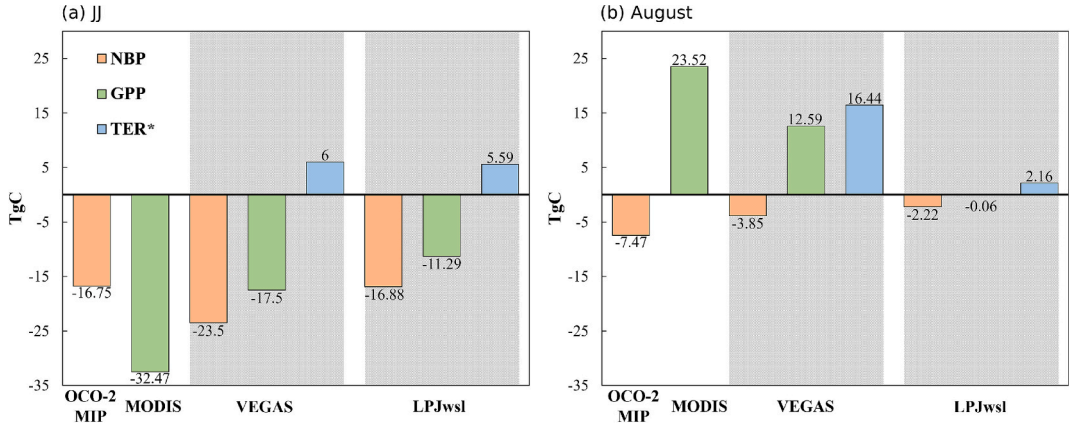

Fig. 4. Regional total anomalies of NBP, GPP, and TER* across different data products within the study region for (a) JJ and (b) August.

Additionally, GPP or net primary productivity (NPP) are commonly used to estimate crop yields due to their theoretical basis and practical applicability, with harvest index (HI) of paddy rice being a key input parameter in estimation models (Wang et al., 2020). Using annual rice yield data from the National Bureau of Statistics, we compute year-on-year percentage changes to evaluate the impact of extreme precipitation on rice yields in 2020, further highlighting its influence on GPP. Fig. 5 illustrates that most provinces experienced declines in rice production, except for Jiangsu and Chongqing, where production remained relatively unchanged (0.08 % and 0.02 %, respectively). Notably, Hubei Province witnessed the largest reduction at − 4.5 %, followed by Zhejiang (−3.2 %) and Anhui (−3.05 %).

3.3. Climate drivers

3.3.1. Contributions of climate drivers to negative NBP anomalies in JJ

The extreme precipitation event in 2020 induced variations in other climate factors, including TAS, VPD, SM, and RAD, which primarily took the responsibility of influenced NBP and its constituent fluxes. To understand these changes and their potential effects on NBP during and after the event, we first examined the spatial patterns of anomalies for these climate elements in JJ and August (Fig. 6).

During JJ, the extreme precipitation on one hand increased SM, particularly in the northern YRV, and elevated relative humidity in the lower troposphere, leading to a decline in VPD (Figs. 6a and b). On the other hand, the persistent rainfall was accompanied by heavy cloud cover, significantly reducing surface RAD and subsequently lowering TAS (Figs. 6c and d).

To quantify the contributions of these climate variations to the negative NBP anomalies during JJ, we applied Equation (6) at each pixel within study area, incorporating NBP anomalies from May as an independent variable to account for legacy effects. The regression models for VEGAS and LPJwsl demonstrated strong explanatory power relatively, with mean R^2 values of 0.75 and 0.69, respectively (Figs. 7a and b). Specifically, the contributions of reduced RAD to NBP reductions were estimated at − 19.36 Tg C for VEGAS (Fig. 7a) and − 8.54 Tg C for LPJwsl (Fig. 7b), highlighting that insufficient RAD during prolonged rainfall suppressed photosynthesis (Chen et al., 2023), thereby weakening terrestrial carbon uptake. Contributions from other climate elements were relatively smaller. Notably, reduced VPD in VEGAS actually enhanced NBP by 10.21 Tg C (Figs. 6b and 7a). Furthermore, we presented spatial patterns for the contributions of each variable (Figs. S2 and S3), suggesting that RAD exerts the widespread inhibitory effect on NBP, particularly in the VEGAS model (Fig. S2c). To validate these results, we also performed a similar MLR analysis for the whole study area. Both equations demonstrated statistical significance as well, with R^2 values of 0.79 for VEGAS and 0.78 for LPJwsl ($p \leq 0.001$ for both models). The RSE were 4.69 Tg C for VEGAS and 3.58 Tg C for LPJwsl, confirming the robustness of the method. The results from the entire study region were consistent with those derived from individual-point models, further confirming that RAD reduction was the dominant factor contributing to negative NBP anomalies during JJ, with absolute t-values exceeding 4 and p-values below 0.001 in both models (Figs. S4a and b).

3.3.2. Contributions of climate drivers to negative NBP anomalies in August

In August, soil memory effects sustained positive SM anomalies, particularly in the northern YRV following the extreme precipitation (Fig. 6e). The dissipation of heavy cloud cover led to a rapid increase in surface RAD (Fig. 6h), which subsequently elevated TAS (Fig. 6g). The rise in TAS enhanced the saturated vapor pressure, causing VPD to return to normal levels and even increase in the southern YRV (Fig. 6f).

We also employed Equation (6) to conduct attribution analysis of negative NBP anomalies in August for both VEGAS and LPJwsl models, yielding mean R^2 values of 0.72 and 0.64, respectively. However, the two equations derived from different models produced divergent results. In the equation derived from VEGAS data, previous negative NBP anomalies were pivotal in impeding NBP recovery, with the contribution of − 9.96 Tg C (Fig. 7c). Recent researches indicate that extreme precipitation events can trigger delayed ecosystem responses, leading to long-term impacts on CO_2 balance (Chen et al., 2017; Hao et al., 2017; Post and Knapp, 2020). These delayed effects, known as the 'legacy effects', were critical in sustaining the negative NBP anomalies observed in August. In contrast, the equation constructed using LPJwsl data underscored the inhibitory effect of TAS (Fig. 7d), contributing − 7.84 Tg C, followed by the legacy effect (−5.68 Tg C). This suggests that the rapid escalation of TAS to positive anomalies was detrimental to vegetation photosynthesis, suppressing carbon sinks. Additionally, the

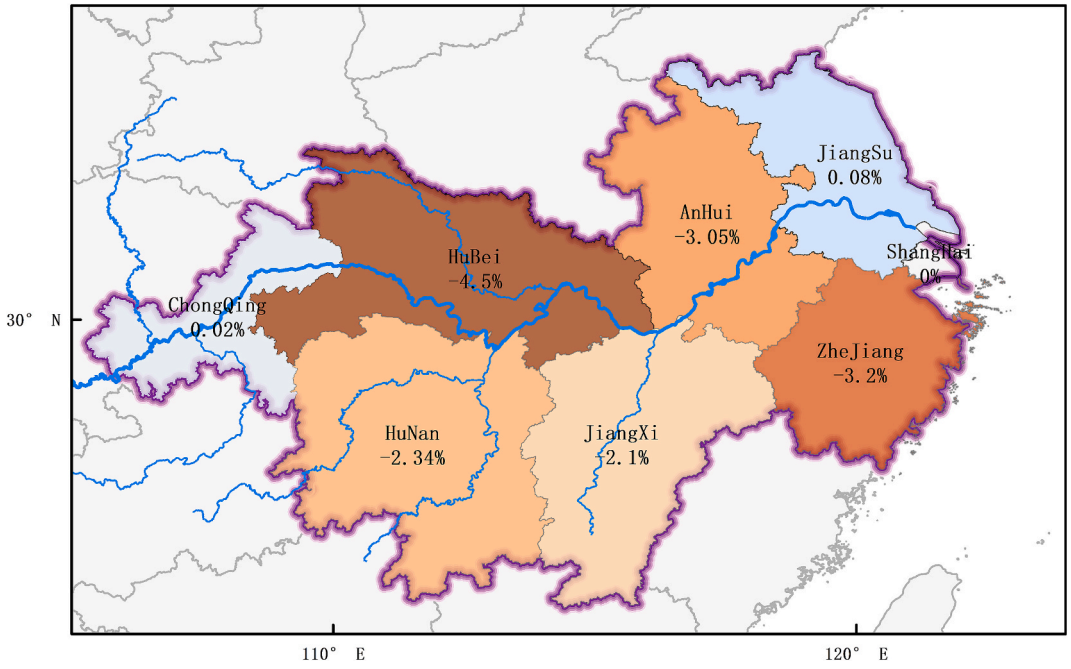

Fig. 5. Year-on-year (YoY) percentage change in annual rice grain production across key provinces within the study area in 2020.

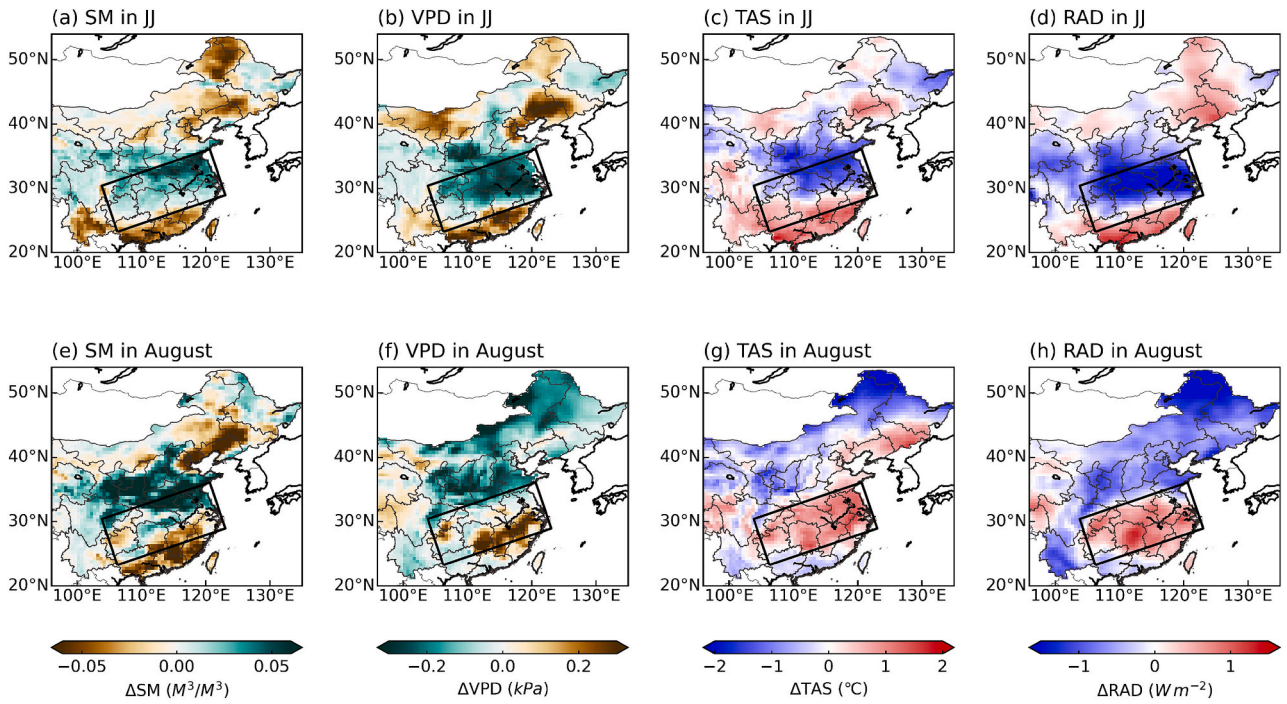

Fig. 6. Anomalies of soil moisture (SM), vapor pressure deficit (VPD), surface air temperature (TAS), and downward solar radiation (RAD) associated with the extreme precipitation in 2020. Panels (a-d) show mean detrended anomalies of SM, VPD, TAS, and RAD during JJ, respectively, while (e-h) represent detrended anomalies for August, respectively.

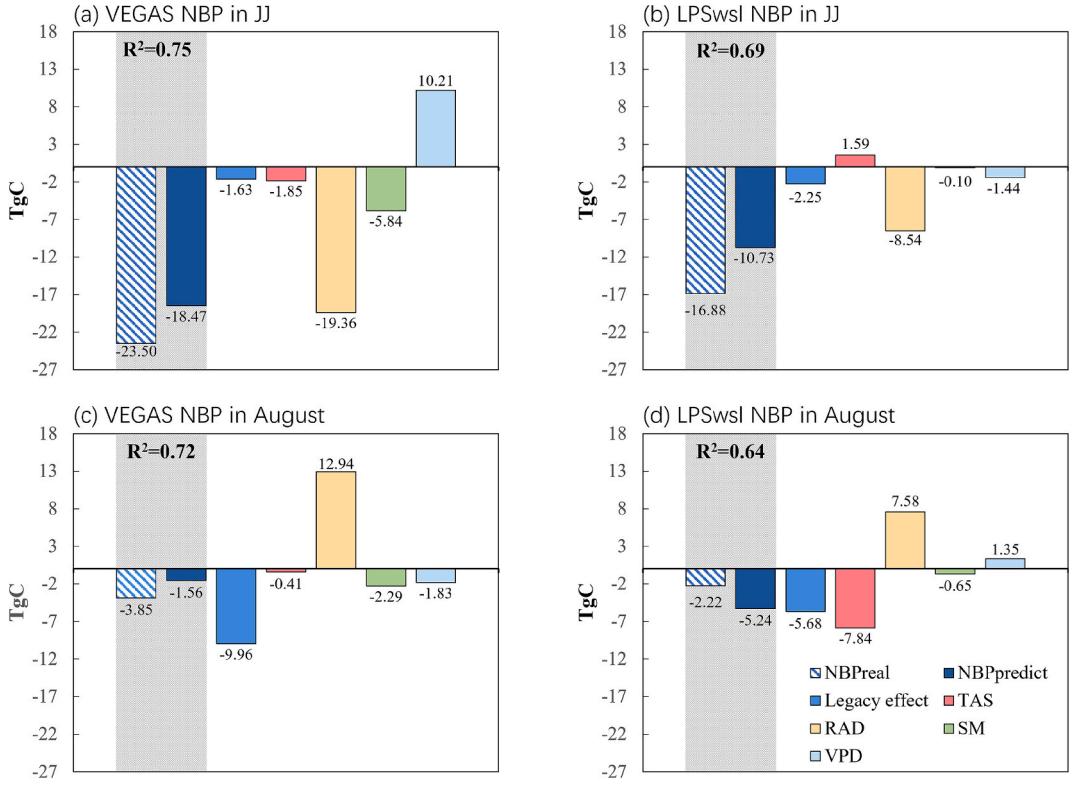

Fig. 7. Contributions of various climate factors to total NBP anomalies within the study region in JJ and August for (a, c) VEGAS and (b, d) LPJwsl.

spatial pattern of contributions from different factors confirmed that legacy effects from the previous month had the greatest impact in VEGAS (Fig. S2h), while TAS exerted the strongest inhibitory effect in LPJwsl (Fig. S3i). For both models, the MLR results across the entire region were generally consistent with these findings, yielding R^2 values of 0.53 and 0.81, respectively. Specifically, the contribution of legacy effect in JJ is − 9.83 Tg C in VEGAS (Fig. S4c), while the contribution of TAS was − 8.38 Tg C in LPJwsl (Fig. S4d), with absolute t-value

exceeding 6 and p-value below 0.001.

3.3.3. Contributions of climate drivers to NBP recovery in August

Based on the attribution analysis, both VEGAS and LPJwsl models identified RAD as the primary driver of NBP recovery, supported by the spatial distribution of contributions (Figs. S2j and S3j). Quantitatively, RAD contributed 12.94 Tg C to NBP recovery in VEGAS and 7.58 Tg C in LPJwsl (Figs. 7c and d). These results suggest that the positive effect of RAD on vegetation photosynthesis was strong enough to overcome previous adversities, enhancing carbon absorption and aiding in recovery. The above conclusions also hold for the results of the overall MLR model. The contribution of RAD is 20.96 Tg C in VEGAS and 8.08 Tg C in LPJwsl (Figs. S4c and d).

4. Discussion

4.1. Significant role of radiation in extreme precipitation events

In the summer of 2020, a record-breaking Meiyu event occurred in YRV, characterized by a prolonged rainy season and abundant precipitation, which inhibited terrestrial ecosystem carbon sequestration. Compared to TER*, GPP variations were the primary drivers of negative NBP anomalies. Excessive precipitation, combined with extensive cloud coverage, led to a significant reduction in solar radiation. The MLR results of both VEGAS and LPJwsl showed consistency in emphasizing the role of RAD, with contributions of approximately −19.36 Tg C for VEGAS and −8.54 Tg C for LPJwsl. These results in line with photosynthetic activity is significantly inhibited by exposure to extreme precipitation due to insufficient photosynthetically active radiation and waterlogging (Chen et al., 2023).

The remarkable recovery of GPP in August facilitated a substantial recovery of NBP, with recovery rate of 55.40 % for OCO-2 v10 MIP, 83.58 % for VEGAS, and 86.85 % for LPJwsl. This recovery was largely driven by increased photosynthetic activity, aided by enhanced solar radiation, as leaf photosynthesis increases nonlinearly with incident photosynthetically active radiation (Mercado et al., 2009). Our study confirms that solar radiation played a pivotal role in both suppressing and recovering NBP, surpassing the effects of SM, VPD, and TAS anomalies. These findings align with previous research indicating that photosynthetic photon flux density (PPFD) is the primary driver of GPP and net ecosystem exchange (NEE) (Njoroge et al., 2022). Increasing temperature appears to be the most important driver of the decline in NBP from 1981 to 2018 globally, when investigating factors influencing net terrestrial carbon uptake (Fernández-Martínez et al., 2023). This contrasts with our findings, which focus on a single extreme event.

Rice, the dominant crop in the study area, is particularly vulnerable to extreme rainfall events. Transplanting is typically completed by June (Zheng, 2015; Chen et al., 2023), and most of rice-producing provinces saw a consistent decline in rice production in 2020. Our MLR analysis of individual pixels highlighted the negative impact of reduced solar radiation (RAD) on carbon absorption, reinforcing previous findings that insufficient solar radiation caused by excessive precipitation leads to yield losses (Tao and Yokozawa, 2005).

4.2. Uncertainty

This study employed multiple linear regression for attribution analysis, future research should explore more advanced models, such as machine learning approaches, to enhance reliability and better understand the climatic drivers of NBP anomalies. Current TBMs still exhibit discrepancies, particularly in how they address the limiting effects of excessive soil moisture on photosynthesis (Li et al., 2019; Pei et al., 2022). Additionally, some studies suggest that state-of-the-art carbon cycle models are overly sensitive to precipitation variability, contributing to uncertainty in the results (Piao et al., 2013). Meanwhile, it is essential to consider the influence of human management practices, such as nitrogen fertilizer application, as they may influence model simulation outcomes to some extent (Kou-Giesbrecht et al., 2025; Reay et al., 2008). Given that extreme precipitation is accompanied by more clouds and fewer clear skies, it inevitably affects the accuracy of remote sensing retrievals and introduces a certain degree of uncertainty to satellite-derived products.

This paper focused on the effects of climatic variables —such as SM, VPD, TAS, and RAD—on NBP reductions and recovery, regardless of the influence of other factors (e.g., nitrogen deposition, wind direction, wind speed). TBMs overlooked the impacts of above-ground biomass changes, soil erosion and waterlogging caused by extreme precipitation. Intense rainfall can damage vegetation, leading to a loss of above-ground biomass and soil organic carbon (Fuhrer et al., 2006). Additionally, prolonged waterlogging may disrupt the root–soil connection, thereby reducing anchorage strength and ultimately resulting in root or stem lodging (Jian et al., 2021). Extreme precipitation events are frequently linked to wind gusts, severe storms, or tropical cyclones. Their impacts include defoliation, branch breakage, and tree mortality, further disrupting carbon sequestration (Frank et al., 2015). Although we accounted for the legacy effects of previous month to some extent, we did not consider the physical damage to vegetation caused by strong winds and heavy precipitation, which could affect both current and subsequent NBP changes. Accurately parameterizing these processes in TBMs is essential to improve our understanding of regional carbon balances, though the lack of sufficient observational data remains a challenge for modelers.

4.3. Implications

The results of this study strongly suggested that extreme precipitation events in 2020 caused significant negative NBP anomalies over the YRV, which aligned with previous findings on the adverse impacts of extreme rainfall on ecosystems, such as in the US Midwest during spring and early summer 2019 (Ford et al., 2021). Located in a humid region with pronounced seasonal rainfall variations, the YRV offered further evidence that extreme rainfall could negatively affect ecosystem productivity and carbon sequestration (Adams et al., 2017; Knapp et al., 2002; Knapp et al., 2008). The substantial decline in GPP during this period led to a marked reduction in carbon sinks, particularly in prolonged flooding conditions, where oxygen deprivation in plant roots can impair respiration and even cause plant death (Kramer et al., 2008).

Under greenhouse gas-induced warming, the intensified hydrological cycle is driving an increase in the frequency and severity of both droughts and heavy precipitation events (Tabari, 2020; Seneviratne et al., 2021), each significantly impacting terrestrial carbon sequestration. Droughts can severely inhibit gross primary productivity (GPP), increase tree mortality, and reduce overall carbon uptake (Deng et al., 2021; Schwalm et al., 2010; van der Molen et al., 2011). Conversely, heavy precipitation events can disrupt carbon dynamics by inducing waterlogging, reducing photosynthesis, and eroding topsoil, leading to significant losses of soil organic carbon (Knapp et al., 2008). Hence, the carbon balance does not exhibit a zero-sum response between these contrasting extremes. While extensive research has explored the impacts of drought on terrestrial carbon sinks, our study underscores the need to also examine the effects of heavy precipitation, as both extremes play critical roles in shaping the future trajectory of the terrestrial carbon cycle.

5. Conclusion

This study examined the variations in NBP over the YRV induced by the record-breading extreme precipitation in 2020, analyzing the underlying mechanisms from the perspectives of biological processes and climate drivers. The unprecedented summer precipitation during JJ led to significant negative NBP anomalies, estimated at approximately − 16.75 Tg C by OCO-2 v10 MIP, −23.50 Tg C by VEGAS, and − 16.88 Tg

C by LPJwsl. Although both negative GPP anomalies and positive TER* anomalies contributed to the anomalous carbon source, the reduction in NBP was primarily driven by the pronounced decline in GPP. Additionally, the decrease in GPP likely contributed to reductions in rice productions across most of provinces over the YRV, particularly in Hubei. With the cessation of the extreme precipitation in August, TER* contributed to the persistence of negative NBP anomalies. Notably, NBP exhibited a rapid recovery in August, primarily driven by a substantial rebound in GPP. Recovery rates were detected as 55.40 % by OCO-2 v10 MIP, 83.58 % by VEGAS, and 86.85 % LPJwsl. MLR analyses at individual grid points suggested reduced RAD as the dominant driver of the decline in NBP during JJ, contributing approximately − 19.36 Tg C in VEGAS and − 8.54 Tg C in LPJwsl. In August, the VEGAS model highlighted negative legacy effects from JJ (−9.96 Tg C), while LPJwsl model emphasized the suppressive effect of abnormally high temperatures (−7.84 Tg C). Results consistently underscored the critical role of RAD in driving the recovery of carbon sink capacity compared to other climatic factors, with contributions of 12.94 Tg C in VEGAS and 7.58 Tg C in LPJwsl. When the entire study area was analyzed as a whole, the attribution findings for both JJ and August aligned with pointwise results, reinforcing the robustness and reliability of the conclusions.

CRediT authorship contribution statement

Zishan Wang: Writing – original draft. **Jun Wang:** Writing – review & editing. **Hao Zhou:** Writing – review & editing. **Qixiang Cai:** Writing – review & editing. **Ran Yan:** Writing – review & editing. **Hongzhao Wang:** Writing – review & editing. **Zhi Huang:** Writing – review & editing. **Meirong Wang:** Writing – review & editing. **Weimin Ju:** Writing – review & editing.

Declaration of competing interest

The authors declare that they have no known competing financial interests or personal relationships that could have appeared to influence the work reported in this paper.

Acknowledgements

This research has been supported by the National Natural Science Foundation of China (grant nos. 42475129 and 42141005); the Natural Science Foundation of Jiangsu Province, China (BK20221449); and the Tibet science and technology innovation base construction project (XZ202401YD0008).

Appendix A. Supplementary data

Supplementary data to this article can be found online at https://doi.org/10.1016/j.jhydrol.2025.134390.

Data availability

GPM precipitation data is available at https://disc.gsfc.nasa.gov/. ERA5 climate data can be accessed at https://www.ecmwf.int/. OCO-2 v10 MIP data is available at https://gml.noaa.gov/ccgg/OCO2_v10mip/index.php. MODIS GPP is available at https://lpdaac.usgs.gov/products/mod17a2hv061/. Jinfo mountain data is available at https://www.nesdc.org.cn. National Bureau of Statistics of China is available from https://data.stats.gov.cn. The SIF dataset from the Sentinel-5P TROPOMI observations is available from https://s5p-troposif.noveltis.fr/data-access/. VEGAS and LPJwsl data will be made available on request.

References

Adams, H.D., et al., 2017. A multi-species synthesis of physiological mechanisms in drought-induced tree mortality. Nat. Ecol. Evol. 1 (9), 1285–1291. https://doi.org/10.1038/s41559-017-0248-x.

Ahmed, F., et al., 2013. Waterlogging tolerance of crops: breeding, mechanism of tolerance, molecular approaches, and future prospects. BioMed Res. Int. 2013, 963525. https://doi.org/10.1155/2013/963525.

Allen, M.R., Ingram, W.J., 2002. Constraints on future changes in climate and the hydrologic cycle. Nature 419 (6903), 224–232. https://doi.org/10.1038/nature01092.

Anjum, M.N., et al., 2018. Performance evaluation of latest integrated multi-satellite retrievals for Global Precipitation Measurement (IMERG) over the northern highlands of Pakistan. Atmos. Res. 205, 134–146. https://doi.org/10.1016/j.atmosres.2018.02.010.

Balashov, N.V., et al., 2023. Flood Impacts on Net Ecosystem Exchange in the Midwestern and Southern United States in 2019. J. Geophys. Res.: Atmos. 128 (18), e2022JD037697. https://doi.org/10.1029/2022JD037697.

Basu, S., et al., 2018. The impact of transport model differences on CO_2 surface flux estimates from OCO-2 retrievals of column average CO_2. Atmos. Chem. Phys. 18 (10), 7189–7215. https://doi.org/10.5194/acp-18-7189-2018.

Basu, S., Nassar, R.J., 2021. Fossil Fuel CO_2 Emissions for the OCO2 Model Intercomparison Project (MIP) [dataset]. https://doi.org/10.5281/zenodo.11210827.

Byrne, B. et al., 2022. Pilot top-down CO2 budget constrained by the v10 OCO-2 MIP Version 1. 10.

Chen, Z., et al., 2017. Extreme rainfall and snowfall alter responses of soil respiration to nitrogen fertilization: a 3-year field experiment. Glob. Change Biol. 23 (8), 3403–3417. https://doi.org/10.1111/gcb.13620.

Chen, H., et al., 2019a. Remote-sensing disturbance detection index to identify spatio-temporal varying flood impact on crop production. Agric. For. Meteorol. 269–270, 180–191. https://doi.org/10.1016/j.agrformet.2019.02.002.

Chen, W., et al., 2019b. Recent Progress in Studies of the Variabilities and Mechanisms of the East Asian Monsoon in a Changing Climate. Adv. Atmos. Sci. 36 (9), 887–901. https://doi.org/10.1007/s00376-019-8230-y.

Chen, X., Wen, Z., Song, Y., Guo, Y., 2022. Causes of extreme 2020 Meiyu-Baiu rainfall: a study of combined effect of Indian Ocean Arctic. Clim. Dyn. 59 (11), 3485–3501. https://doi.org/10.1007/s00382-022-06279-0.

Chen, J., Qiu, B., Guo, W., Li, L., Miao, X., 2023. Divergent response of crops and natural vegetation to the record-breaking extreme precipitation event in 2020 modulated by topography. Environ. Res. Lett. 18. https://doi.org/10.1088/1748-9326/acdaae.

Chevallier, F., Feng, L., Bösch, H., Palmer, P.I., Rayner, P.J., 2010. On the impact of transport model errors for the estimation of CO_2 surface fluxes from GOSAT observations. Geophys. Res. Lett. 37 (21). https://doi.org/10.1029/2010GL044652.

Cornwall, W., 2021. Europe's deadly floods leave scientists stunned. Science 373 (6553), 372–373. https://doi.org/10.1126/science.373.6553.372.

Dalagnol, R., et al., 2022. Extreme rainfall and its impacts in the Brazilian Minas Gerais state in January 2020: can we blame climate change? Clim. Resil. Sustain. 1 (1), e15. https://doi.org/10.1002/cli2.15.

Deng, Y., et al., 2021. Responses of vegetation greenness and carbon cycle to extreme droughts in China. Agr. Forest Meteorol. 298–299, 108307. https://doi.org/10.1016/j.agrformet.2020.108307.

Ding, Y., 2004. Seasonal March of the East-Asian Summer Monsoon. East Asian Monsoon, pp. 3–53. https://doi.org/10.1142/9789812701411_0001.

Dinsmore, K.J., Billett, M.F., Dyson, K.E., 2013. Temperature and precipitation drive temporal variability in aquatic carbon and GHG concentrations and fluxes in a peatland catchment. Glob. Change Biol. 19 (7), 2133–2148. https://doi.org/10.1111/gcb.12209.

Donat, M.G., Lowry, A.L., Alexander, L.V., O'Gorman, P.A., Maher, N., 2016. More extreme precipitation in the world's dry and wet regions. Nat. Clim. Change 6 (5), 508–513. https://doi.org/10.1038/nclimate2941.

Fan, L., et al., 2022. Evaluation of satellite and reanalysis estimates of surface and root-zone soil moisture in croplands of Jiangsu Province, China. Remote Sens. Environ. 282, 113283. https://doi.org/10.1016/j.rse.2022.113283.

Fernández-Martínez, M., et al., 2023. Diagnosing destabilization risk in global land carbon sinks. Nature 615 (7954), 848–853. https://doi.org/10.1038/s41586-023-05725-1.

Ford, T.W., Chen, L., Schoof, J.T., 2021. Variability and transitions in precipitation extremes in the Midwest United States. J. Hydrometeorol. 22 (3), 533–545. https://doi.org/10.1175/JHM-D-20-0216.1.

Frank, D., et al., 2015. Effects of climate extremes on the terrestrial carbon cycle: concepts, processes and potential future impacts. Glob. Change Biol. 21 (8), 2861–2880. https://doi.org/10.1111/gcb.12916.

Fuhrer, J., et al., 2006. Climate risks and their impact on agriculture and forests in Switzerland. Climate Variability, Predictability and Climate Risks. A European Perspective, pp. 79–102. https://doi.org/10.1007/978-1-4020-5714-4_5.

Giorgi, F., Raffaele, F., Coppola, E., 2019. The response of precipitation characteristics to global warming from climate projections. Earth Syst. Dynam. 10 (1), 73–89. https://doi.org/10.5194/esd-10-73-2019.

Goldewijk, C.G.M.K., 2017. Anthropogenic land-use estimates for the Holocene; HYDE 3.2. DANS Data Station Archaeology. https://doi.org/10.17026/DANS-25G-GEZ3.

Guanter, L., et al., 2014. Global and time-resolved monitoring of crop photosynthesis with chlorophyll fluorescence. Proc. Natl. Acad. Sci. 111 (14), E1327–E1333. https://doi.org/10.1073/pnas.1320008111.

Hao, Y.B., et al., 2017. Aboveground net primary productivity and carbon balance remain stable under extreme precipitation events in a semiarid steppe ecosystem.

Agric. For. Meteorol. 240–241, 1–9. https://doi.org/10.1016/j.agrformet.2017.03.006.
Harris, I., Osborn, T.J., Jones, P., Lister, D., 2020. Version 4 of the CRU TS monthly high-resolution gridded multivariate climate dataset. Sci. Data 7 (1), 109. https://doi.org/10.1038/s41597-020-0453-3.
He, B., et al., 2022. Worldwide impacts of atmospheric vapor pressure deficit on the interannual variability of terrestrial carbon sinks. Natl. Sci. Rev. 9 (4), nwab150. https://doi.org/10.1093/nsr/nwab150.
Hersbach, H., et al., 2020. The ERA5 global reanalysis. Q. J. Roy. Meteor. Soc. 146 (730), 1999–2049. https://doi.org/10.1002/qj.3803.
Hilton, R.G., et al., 2008. Tropical-cyclone-driven erosion of the terrestrial biosphere from mountains. Nat. Geosci. 1 (11), 759–762. https://doi.org/10.1038/ngeo333.
Intergovernmental Panel on Climate, C., 2023. Climate Change 2021 – The Physical Science Basis: Working Group I Contribution to the Sixth Assessment Report of the Intergovernmental Panel on Climate Change. Cambridge University Press, Cambridge.
Jian, Y., Fu, J., Zhou, F., 2021. A review of studies on the impacts of extreme precipitation on rice yields. Prog. Geogr. 40 (10), 1746–1760. https://doi.org/10.18306/dlkxjz.2021.10.011.
Jiao, W., Wang, L., McCabe, M.F., 2021. Multi-sensor remote sensing for drought characterization: current status, opportunities and a roadmap for the future. Remote Sens. Environ. 256, 112313. https://doi.org/10.1016/j.rse.2021.112313.
Knapp, A.K., et al., 2002. Rainfall variability, carbon cycling, and plant species diversity in a mesic grassland. Science 298 (5601), 2202–2205. https://doi.org/10.1126/science.1076347.
Knapp, A.K., et al., 2008. Consequences of more extreme precipitation regimes for terrestrial ecosystems. BioScience 58 (9), 811–821. https://doi.org/10.1641/B580908.
Köhler, P., et al., 2018. Global retrievals of solar-induced chlorophyll fluorescence with TROPOMI: first results and intersensor comparison to OCO-2. Geophys. Res. Lett. 45 (19), 10,456–10,463. https://doi.org/10.1029/2018GL079031.
Köhler, P., et al., 2020. Global retrievals of solar-induced chlorophyll fluorescence at red wavelengths with TROPOMI. Geophys. Res. Lett. 47 (15), e2020GL087541. https://doi.org/10.1029/2020GL087541.
Kou-Giesbrecht, S., et al., 2025. Rising nitrogen deposition leads to only a minor increase in CO_2 uptake in Earth system models. Commun. Earth Environ. 6 (1), 216. https://doi.org/10.1038/s43247-024-01943-1.
Kramer, K., Vreugdenhil, S.J., van der Werf, D.C., 2008. Effects of flooding on the recruitment, damage and mortality of riparian tree species: a field and simulation study on the Rhine floodplain. For. Ecol. Manage. 255 (11), 3893–3903. https://doi.org/10.1016/j.foreco.2008.03.044.
Li, M., Wu, P., Ma, Z., 2020. A comprehensive evaluation of soil moisture and soil temperature from third-generation atmospheric and land reanalysis data sets. Int. J. Climatol. 40 (13), 5744–5766. https://doi.org/10.1002/joc.6549.
Li, W., et al., 2022. Widespread increasing vegetation sensitivity to soil moisture. Nat. Commun. 13 (1), 3959. https://doi.org/10.1038/s41467-022-31667-9.
Li, X., Xiao, J., 2020. Global climatic controls on interannual variability of ecosystem productivity: similarities and differences inferred from solar-induced chlorophyll fluorescence and enhanced vegetation index. Agric. For. Meteorol. 288–289, 108018. https://doi.org/10.1016/j.agrformet.2020.108018.
Li, Y., Guan, K., Schnitkey, G.D., DeLucia, E., Peng, B., 2019. Excessive rainfall leads to maize yield loss of a comparable magnitude to extreme drought in the United States. Glob. Change Biol. 25 (7), 2325–2337. https://doi.org/10.1111/gcb.14628.
Liu, C., et al., 2023. Extreme Mei-yu in 2020: characteristics, causes, predictability and perspectives. Earth-Sci. Rev. 246, 104597. https://doi.org/10.1016/j.earscirev.2023.104597.
Ma, X., et al., 2016. Drought rapidly diminishes the large net CO_2 uptake in 2011 over semi-arid Australia. Sci. Rep. 6 (1), 37747. https://doi.org/10.1038/srep37747.
Mercado, L.M., et al., 2009. Impact of changes in diffuse radiation on the global land carbon sink. Nature 458 (7241), 1014–1017. https://doi.org/10.1038/nature07949.
Muñoz-Sabater, J., et al., 2021. ERA5-Land: a state-of-the-art global reanalysis dataset for land applications. Earth Syst. Sci. Data 13 (9), 4349–4383. https://doi.org/10.5194/essd-13-4349-2021.
Njoroge, B., et al., 2022. Carbon flux variation and associated biomass energy storage economic value implications in the Dinghushan Biosphere Reserve. J. Clean. Prod. 376, 134274. https://doi.org/10.1016/j.jclepro.2022.134274.
Oda, T., Maksyutov, S., Andres, R.J., 2018. The Open-source Data Inventory for Anthropogenic CO2, version 2016 (ODIAC2016): a global monthly fossil fuel CO2 gridded emissions data product for tracer transport simulations and surface flux inversions. Earth Syst. Sci. Data 10 (1), 87–107. https://doi.org/10.5194/essd-10-87-2018.
Pan, X., Li, T., Sun, Y., Zhu, Z., 2021. Cause of extreme heavy and persistent rainfall over Yangtze River in summer 2020. Adv. Atmos. Sci. 38 (12), 1994–2009. https://doi.org/10.1007/s00376-021-0433-3.
Pei, Y., et al., 2022. Evolution of light use efficiency models: improvement, uncertainties, and implications. Agric. For. Meteorol. 317, 108905. https://doi.org/10.1016/j.agrformet.2022.108905.
Peiro, H., et al., 2022. Four years of global carbon cycle observed from the Orbiting Carbon Observatory 2 (OCO-2) version 9 and in situ data and comparison to OCO-2 version 7. Atmos. Chem. Phys. 22 (2), 1097–1130. https://doi.org/10.5194/acp-22-1097-2022.
Pendergrass, A.G., Hartmann, D.L., 2014. Changes in the distribution of rain frequency and intensity in response to global warming. J. Clim. 27 (22), 8372–8383. https://doi.org/10.1175/JCLI-D-14-00183.1.
Piao, S., et al., 2013. Evaluation of terrestrial carbon cycle models for their response to climate variability and to CO_2 trends. Glob. Change Biol. 19 (7), 2117–2132. https://doi.org/10.1111/gcb.12187.
Piao, S., et al., 2019. The impacts of climate extremes on the terrestrial carbon cycle: a review. Sci. China Earth Sci. 62 (10), 1551–1563. https://doi.org/10.1007/s11430-018-9363-5.
Post, A.K., Knapp, A.K., 2020. The importance of extreme rainfall events and their timing in a semi-arid grassland. J. Ecol. 108 (6), 2431–2443. https://doi.org/10.1111/1365-2745.13478.
Poulter, B., et al., 2011. Plant functional type mapping for earth system models. Geosci. Model Dev. 4 (4), 993–1010. https://doi.org/10.5194/gmd-4-993-2011.
Prakash, S., 2019. Performance assessment of CHIRPS, MSWEP, SM2RAIN-CCI, and TMPA precipitation products across India. J. Hydrol. 571, 50–59. https://doi.org/10.1016/j.jhydrol.2019.01.036.
Qi, Y., Zhang, R., Wang, Z., 2023. Large-scale background and role of quasi-biweekly moisture transport in the extreme Yangtze River rainfall in summer 2020. Clim. Dynam. 61 (7), 3721–3736. https://doi.org/10.1007/s00382-023-06774-y.
Qian, H., Joseph, R., Zeng, N., 2008. Response of the terrestrial carbon cycle to the El Nĩ no-Southern Oscillation. Tellus B 60 (4), 537–550. https://doi.org/10.1111/j.1600-0889.2008.00360.x.
Reay, D.S., Dentener, F., Smith, P., Grace, J., Feely, R.A., 2008. Global nitrogen deposition and carbon sinks. Nat. Geosci. 1 (7), 430–437. https://doi.org/10.1038/ngeo230.
Rogers, A., 2014. The use and misuse of V c, max in Earth System Models. Photosynth. Res. 119 (1), 15–29. https://doi.org/10.1007/s11120-013-9818-1.
Rogers, A., Medlyn, B.E., Dukes, J.S., 2014. Improving representation of photosynthesis in. Earth System Models. New Phytol. 204 (1), 12–14. https://doi.org/10.1111/nph.12972.
Schuh, A.E., et al., 2019. Quantifying the impact of atmospheric transport uncertainty on CO_2 surface flux estimates. Global Biogeochem. Cy. 33 (4), 484–500. https://doi.org/10.1029/2018GB006086.
Schwalm, C.R., et al., 2010. Assimilation exceeds respiration sensitivity to drought: a FLUXNET synthesis. Glob. Change Biol. 16 (2), 657–670. https://doi.org/10.1111/j.1365-2486.2009.01991.x.
Seneviratne, S.I. et al., 2021. Weather and climate extreme events in a changing climate. Climate Change 2021: The Physical Science Basis. Contribution of Working Group I to the Sixth Assessment Report of the Intergovernmental Panel on Climate Change. pp. 1513–1766. https://doi.org/10.1017/9781009157896.013.
Sitch, S., et al., 2003. Evaluation of ecosystem dynamics, plant geography and terrestrial carbon cycling in the LPJ dynamic global vegetation model. Glob. Change Biol. 9 (2), 161–185. https://doi.org/10.1046/j.1365-2486.2003.00569.x.
Sitch, S., et al., 2015. Recent trends and drivers of regional sources and sinks of carbon dioxide. Biogeosciences 12 (3), 653–679. https://doi.org/10.5194/bg-12-653-2015.
Tabari, H., 2020. Climate change impact on flood and extreme precipitation increases with water availability. Sci. Rep. 10 (1), 13768. https://doi.org/10.1038/s41598-020-70816-2.
Tao, F., Yokozawa, M., 2005. Risk analyses of rice yield to seasonal climate variability in China. J. Agric. Meteorol. 60 (5), 885–887. https://doi.org/10.2480/agrmet.885.
Turner, D.P., et al., 2006. Evaluation of MODIS NPP and GPP products across multiple biomes. Remote Sens. Environ. 102 (3), 282–292. https://doi.org/10.1016/j.rse.2006.02.017.
van der Molen, et al., 2011. Drought and ecosystem carbon cycling. Agric. For. Meteorol. 151 (7), 765–773. https://doi.org/10.1016/j.agrformet.2011.01.018.
Walther, S., et al., 2019. Satellite observations of the contrasting response of trees and grasses to variations in water availability. Geophys. Res. Lett. 46 (3), 1429–1440. https://doi.org/10.1029/2018GL080535.
Wang, F., et al., 2020. Rice yield estimation based on an NPP model with a changing harvest index. IEEE J. Sel. Top. Appl. Earth Obs. Remote Sens. 13, 2953–2959. https://doi.org/10.1109/JSTARS.2020.2993905.
Wang, J., et al., 2018a. Improved modeling of gross primary productivity (GPP) by better representation of plant phenological indicators from remote sensing using a process model. Ecol. Indic. 88, 332–340. https://doi.org/10.1016/j.ecolind.2018.01.042.
Wang, J., et al., 2018b. Contrasting terrestrial carbon cycle responses to the 1997/98 and 2015/16 extreme El Niño events. Earth Syst. Dynam. 9 (1), 1–14. https://doi.org/10.5194/esd-9-1-2018.
Wang, J., et al., 2023. Anomalous net biome exchange over Amazonian rainforests induced by the 2015/16 El Niño: soil dryness-shaped spatial pattern but temperature-dominated total flux. Geophys. Res. Lett. 50 (11), e2023GL103379. https://doi.org/10.1029/2023GL103379.
Wang, J., Zeng, N., Wang, M., 2016. Interannual variability of the atmospheric CO_2 growth rate: roles of precipitation and temperature. Biogeosciences 13, 2339–2352. https://doi.org/10.5194/bg-13-2339-2016.
Wang, S., Zhang, Y., Ju, W., Qiu, B., Zhang, Z., 2021. Tracking the seasonal and inter-annual variations of global gross primary production during last four decades using satellite near-infrared reflectance data. Sci. Total Environ. 755, 142569. https://doi.org/10.1016/j.scitotenv.2020.142569.
Wang, Y., Wang, S., Luo, F., Wang, H., 2022. Strengthened impacts of Indian Ocean dipole on the Yangtze precipitation contribute to the extreme rainfall of 2020 Meiyu season. J. Geophys. Res.: Atmos. 127 (24), e2022JD037028. https://doi.org/10.1029/2022JD037028.
Yildirim, E., Demir, I., 2022. Agricultural flood vulnerability assessment and risk quantification in Iowa. Sci. Total Environ. 826, 154165. https://doi.org/10.1016/j.scitotenv.2022.154165.
Yin, Y., et al., 2020. Cropland carbon uptake delayed and reduced by 2019 Midwest floods. AGU Adv. 1 (1), e2019AV000140. https://doi.org/10.1029/2019AV000140.

Yu, L., Leng, G., Python, A., Peng, J., 2021. A comprehensive evaluation of latest GPM IMERG V06 early, late and final precipitation products across China. Remote Sens. https://doi.org/10.3390/rs13061208.

Zeng, N., Mariotti, A., Wetzel, P., 2005. Terrestrial mechanisms of interannual CO_2 variability. Global Biogeochem. Cy. 19 (1). https://doi.org/10.1029/2004GB002273.

Zeng, N., et al., 2014. Agricultural Green Revolution as a driver of increasing atmospheric CO_2 seasonal amplitude. Nature 515 (7527), 394–397. https://doi.org/10.1038/nature13893.

Zeppel, M.J.B., Wilks, J.V., Lewis, J.D., 2014. Impacts of extreme precipitation and seasonal changes in precipitation on plants. Biogeosciences 11 (11), 3083–3093. https://doi.org/10.5194/bg-11-3083-2014.

Zhang, C., et al., 2023. Construction of multi-extreme climate events composite grads index and comprehensive analysis of extreme climate in the Yangtze River Basin from 1961 to 2020. Chinese J. Geophys. (in Chinese) 66 (3), 920–938. https://doi.org/10.6038/cjg2022Q0255.

Zhang, R., 2015. Changes in East Asian summer monsoon and summer rainfall over eastern China during recent decades. Sci. Bull. 60 (13), 1222–1224. https://doi.org/10.1007/s11434-015-0824-x.

Zhang, R., Min, Q., Su, J., 2017. Impact of El Niño on atmospheric circulations over East Asia and rainfall in China: role of the anomalous western North Pacific anticyclone. Sci. China-Earth Sci. 1124–1132. https://doi.org/10.1007/s11430-016-9026-x.

Zhang, W., et al., 2021. Increasing precipitation variability on daily-to-multiyear time scales in a warmer world. Sci. Adv. 7 (31), eabf8021. https://doi.org/10.1126/sciadv.abf8021.

Zhang, W., Zheng, C., Song, Z., Deng, A., He, Z., 2015. Farming systems in China: innovations for sustainable crop production. Crop Physiology, second ed. Academic Press, San Diego, pp. 43–64. https://doi.org/10.1016/B978-0-12-417104-6.00003-0.

Zhang, Y., Ye, A., 2021. Would the obtainable gross primary productivity (GPP) products stand up? A critical assessment of 45 global GPP products. Sci. Total Environ. 783, 146965. https://doi.org/10.1016/j.scitotenv.2021.146965.

Zhang, Z., et al., 2018. Enhanced response of global wetland methane emissions to the 2015–2016 El Niño-Southern Oscillation event. Environ. Res. Lett. 13 (7), 074009. https://doi.org/10.1088/1748-9326/aac939.

Zheng, Y., 2015. Research on the Spatial-temporal distribution of growth period of main grain crops and its change in China.